Mechatronics 77 (2021) 102599

Contents lists available at ScienceDirect

Mechatronics

journal homepage: www.elsevier.com/locate/mechatronics

Anti-swing control of a hydraulic loader crane with a hanging load ☆

Konrad Johan Jensen *, Morten Kjeld Ebbesen, Michael Rygaard Hansen

Department of Engineering Sciences, University of Agder, 4879 Grimstad, Norway

ARTICLE INFO

Keywords:
Loader crane
Anti-swing
Hydraulics
Kinematics
Feedforward

ABSTRACT

In this paper, anti-swing control for a hydraulic loader crane is presented. The difference between hydraulic and electric cranes are discussed to show the challenges associated with hydraulic actuation. The hanging load dynamics and relevant kinematics of the crane are derived to create the 2-DOF anti-swing controller. The anti-swing controller is added to the electro-hydraulic motion controller via feedforward. A dynamic simulation model of the crane is made, and the control system is evaluated in simulations with a path controller in actuator space. Simulation results show significant reduction in the load swing angle during motion. Experiments are carried out to verify the performance of the anti-swing controller, showing good suppression of the payload angle in practice.

1. Introduction

Anti-swing control is an extensively studied topic, with applications to cranes and hoists in factories, shipyards, and warehouses etc. However, any non-stationary lifting equipment will induce undesirable load swing in the hanging load when moving. This load swing can increase cycle times, reduce efficiency, and in the worst case lead to safety hazards and accidents. Various techniques have been tested to suppress load swing. This is a difficult task, as systems with hanging loads are underactuated, meaning the degrees of freedom are greater than the number of controlled actuators.

Typically the anti-swing controllers are implemented on electric overhead cranes, where one or several servomotors control the translational motion of the crane. The control system typically consists of two feedback controllers, one controlling the position of the crane and the other controlling the load swing. Early work on anti-swing control of overhead cranes includes [1–4], where linearized models are utilized. More advanced control systems including fuzzy logic, sliding mode, and robust control can be found in [5–16], where a nonlinear model of the crane is often used.

A method that can be used both for anti-swing and vibration reduction in flexible systems is input shaping. Based on system dynamics, for example bandwidth and damping ratio, an input signal is designed to be self-canceling [17–19].

Another similar method is called delayed reference control. In this case the reference generator is time shifted based on the measured payload angle [20,21].

Anti-swing control for hydraulic cranes is not an extensively studied area, but references include [22] which investigates tool-point control and anti-swing for a planar hydraulic crane.

For this paper, a hydraulic loader crane is considered, shown in Fig. 2. In this case the load is hanging from the crane tip, instead of the trolley of an overhead crane. Many hydraulic cranes use pressure compensated valves, which give a load independent velocity control for each actuator. For closed loop control systems, the load independent velocity control can be utilized in a control system using feedforward [23,24]. In this case, both a position reference and a velocity reference are generated in the control system. An example of a typical closed loop electro-hydraulic motion control system with feedforward (FF) and feedback (FB) is shown in Fig. 1.

The focus of this paper is on how to design anti-swing control for hydraulically actuated cranes. This paper presents a novel anti-swing controller which utilizes load independent velocity control in combination with kinematic transformations. Based on this, the novel method provides reference motion for the individual hydraulic degrees of freedom by combining contributions from a path controller and an anti-swing controller.

2. Considered system

In this paper an HMF 2020K4 loader crane is used as a case study for modeling, simulation, and experiments. Fig. 2 shows the main components of the HMF 2020K4 loader crane. Both the main cylinder and knuckle cylinder are used to compensate for the hanging

☆ This paper was recommended for publication by Associate Editor Peter Hehenberger.

* Corresponding author.
E-mail addresses: konrad.j.jensen@uia.no (K.J. Jensen), morten.k.ebbesen@uia.no (M.K. Ebbesen), michael.r.hansen@uia.no (M.R. Hansen).

https://doi.org/10.1016/j.mechatronics.2021.102599
Received 25 January 2021; Received in revised form 3 May 2021; Accepted 6 June 2021
Available online 20 June 2021

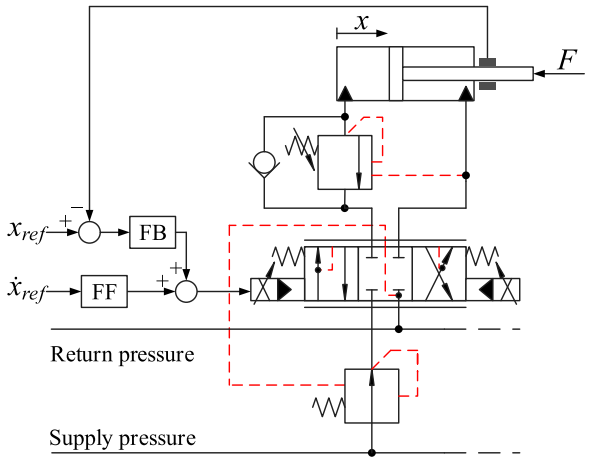

Fig. 1. Electro-hydraulic motion control system with feedforward.

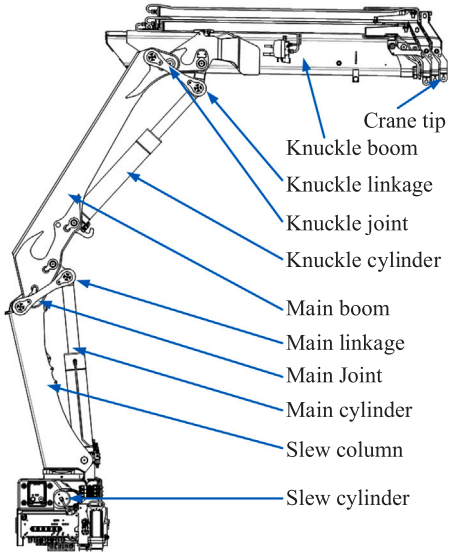

Fig. 2. Main components of the considered crane.

load dynamics. The relevant data for the main cylinder and knuckle cylinder are shown in Table 1. Each actuator is controlled via a pressure compensated proportional directional valve which ensures load independent flow control of the actuators. Counterbalance valves are also used for load holding, assisting in lowering of the booms, and pressure relief of pressure surges. An illustration of the hydraulic system for the knuckle cylinder is shown in Fig. 3. Fig. 4 shows the hanging load definitions along with the main boom angle θ_m, knuckle boom angle θ_k, and payload angle θ_p.

2.1. Difference from electric overhead cranes

Since research in anti-swing control of electric overhead cranes is an extensively studied subject, the differences between electric and hydraulic cranes are discussed in this section.

The difference in actuation is clear, an electric motor exerts a torque on the load based the motor current, while the hydraulic cylinder exerts a force on the load based on the hydraulic pressure. For some hydraulic systems, including the HMF 2020K4 loader crane, the pressure compensator senses the load pressure and automatically adjusts the pressure drop over the control valve to give load independent flow control. As a result, the hydraulic system is able to control the velocity of the load

Table 1
Data for the main cylinder and knuckle cylinder.

Description	Name	Value
Main piston diameter	$D_{p,m}$	0.16 m
Main piston area	A_m	0.0201 m^2
Main rod diameter	$D_{r,m}$	0.1 m
Main annulus area	$A_{a,m}$	0.0123 m^2
Main piston area ratio	$\phi_m = \frac{A_{a,m}}{A_m}$	0.6094
Main valve maximum flow	$Q_{max,m}$	40 l/min
Knuckle piston diameter	$D_{p,k}$	0.15 m
Knuckle piston area	A_k	0.0177 m^2
Knuckle rod diameter	$D_{r,k}$	0.1 m
Knuckle annulus area	$A_{a,k}$	0.0098 m^2
Knuckle piston area ratio	$\phi_k = \frac{A_{a,k}}{A_k}$	0.5556
Knuckle valve maximum flow	$Q_{max,k}$	40 l/min

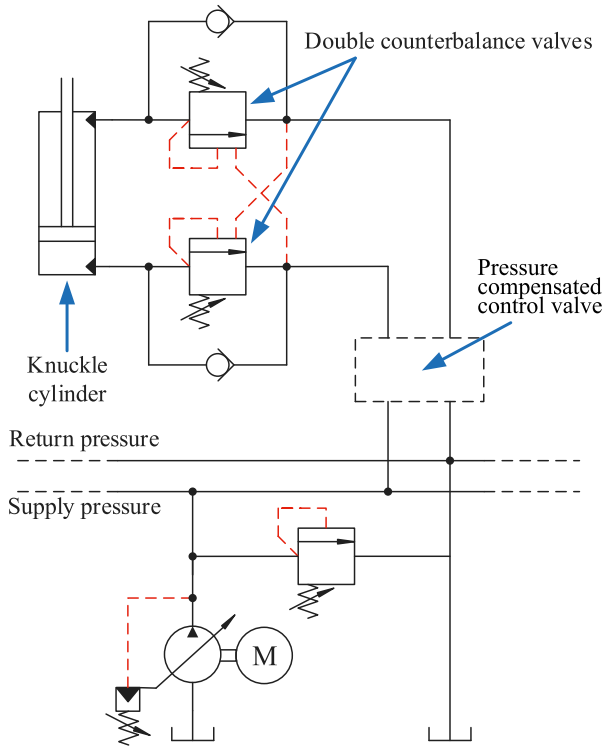

Fig. 3. Hydraulic circuit for the knuckle cylinder..

directly, whereas the electric system controls the force applied to the load.

Fig. 5 illustrates a typical overhead crane where the hanging load is connected to a trolley. The trolley is only able to move in the x-direction, and the electric motor exerts a force F_{motor} on the trolley through the wheels. The applied force affects both the trolley motion and payload motion, and is used to control the position along the x-axis as well as the payload angle θ_p.

2.2. Control strategy

The control strategy suggested in this paper is shown in Fig. 6. This control strategy is useful for any hydraulically actuated manipulator with a tool point and a number of joint angles controlled by means of hydraulic cylinders. This constitute a wide variety of load handling machinery. The main task is position control of the tool point and, classically, this may be combined with a velocity feedforward term. Feedback control is most easily implemented with reference to the actuator motion [25]. Therefore, inverse kinematics is employed to transfer from tool point coordinates via joint coordinates to actuator

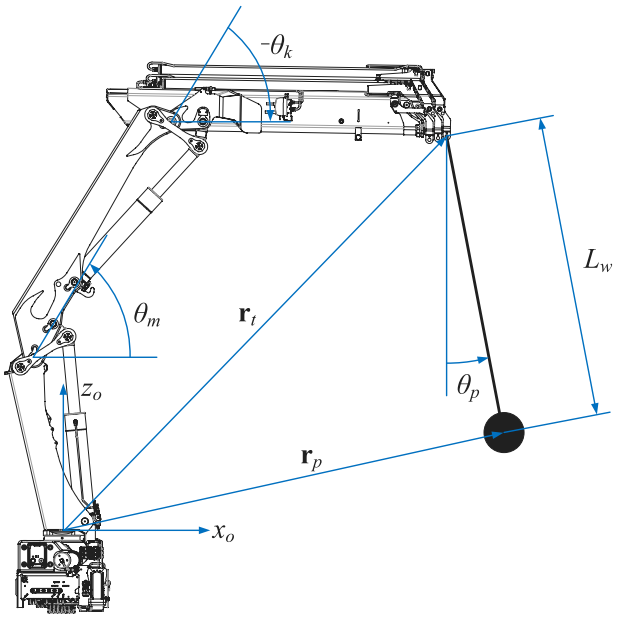

Fig. 4. Definitions of crane tip and hanging load geometries.

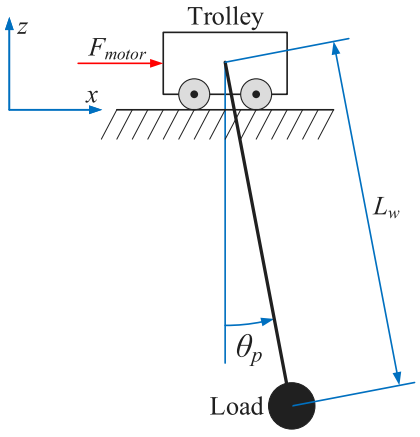

Fig. 5. Typical overhead crane with hanging load.

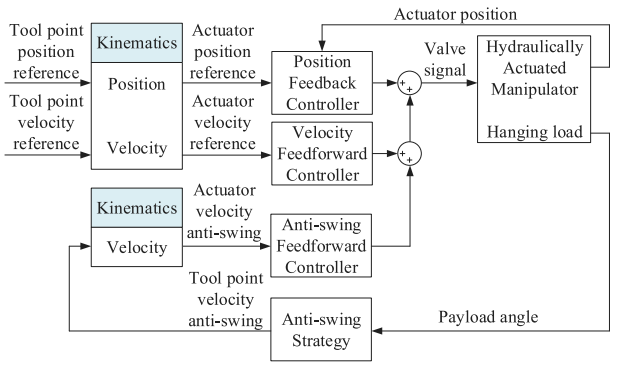

Fig. 6. Anti-swing control strategy.

coordinates. The anti-swing effort is introduced in parallel with the feedforward term, but is computed with the purpose of counteracting the continuously measured payload angle by adjusting the tool point velocity. Therefore, the anti-swing effort also requires a kinematic transformation into actuator space.

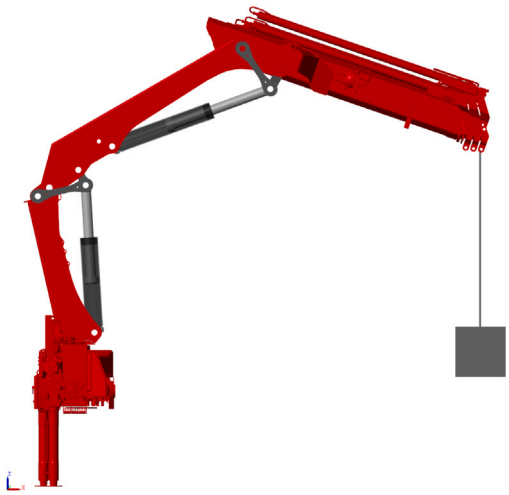

Fig. 7. 2D view of the crane model in MATLAB Simscape™.

The proposed control strategy can be implemented in several ways. In general, any tool point reference motion will be either 2-dimensional or 3-dimensional. For the 2-dimensional case, a minimum of two actuators is required, however, more may be employed yielding some degree of redundancy that can be handled by means of optimization within the null-space, see [26].

In this paper, only 2-dimensional motion is considered leaving four different possible combinations:

1. Main boom actuator and knuckle boom actuator
2. Main boom actuator and telescope actuator
3. Knuckle boom actuator and telescope actuator
4. Main boom actuator, knuckle boom actuator and telescope actuator.

To illustrate the presented control strategy, the necessary kinematic transformations together with the anti swing strategy have been developed and implemented for case 1.

3. System modeling

A dynamic model of the crane has been made in MATLAB Simscape™. 3D CAD models have been imported into the model using the Multibody library, and the hydraulic system has been modeled using the hydraulic library. A side view of the crane in the simulation model is shown in Fig. 7.

3.1. Hanging load dynamics

To derive the equations of motion for the hanging load using the payload angle θ_p, the Euler–Lagrange equations are used. For the following equations, the notation $s_{\theta_p} = \sin(\theta_p)$, $c_{\theta_p} = \cos(\theta_p)$ is used. With the boom tip position defined as $\mathbf{r}_t = [x_t \; z_t]^T$, the payload position can be calculated as follows.

$$\mathbf{r}_p = \mathbf{r}_t + L_w \cdot \begin{bmatrix} s_{\theta_p} \\ -c_{\theta_p} \end{bmatrix} \tag{1}$$

Assuming constant wire length, the payload velocity can be calculated by taking the time derivative of the payload position, shown in Eq. (2).

$$\dot{\mathbf{r}}_p = \dot{\mathbf{r}}_t + L_w \cdot \dot{\theta}_p \cdot \begin{bmatrix} c_{\theta_p} \\ s_{\theta_p} \end{bmatrix} \tag{2}$$

The Lagrangian $\mathcal{L}$ of the system is defined as the kinetic energy minus the potential energy, and is shown in Eq. (3).

$$\mathcal{L} = \mathcal{K} - \mathcal{P} \tag{3}$$

The kinetic energy of the payload is:

$$\mathcal{K} = \frac{1}{2} \cdot m_p \cdot \dot{\mathbf{r}}_p^T \cdot \dot{\mathbf{r}}_p \tag{4}$$

The potential energy of the payload is:

$$\mathcal{P} = m_p \cdot g \cdot \left(z_t - L_w \cdot c_{\theta_p} \right) \tag{5}$$

The total Lagrangian of the payload is then calculated in Eq. (6).

$$\begin{aligned} \mathcal{L} = \frac{1}{2} \cdot m_p \cdot \Big(& \dot{x}_t^2 + L_w^2 \cdot \dot{\theta}_p^2 + 2 \cdot \dot{x}_t \cdot L_w \cdot \dot{\theta}_p \cdot c_{\theta_p} \\ & + \dot{z}_t^2 + 2 \cdot \dot{z}_t \cdot L_w \cdot \dot{\theta}_p \cdot s_{\theta_p} \Big) \\ & - m_p \cdot g \cdot \left(z_t - L_w \cdot c_{\theta_p} \right) \end{aligned} \tag{6}$$

The equation of motion of the payload described by the coordinate θ_p is given by the Euler–Lagrange equation below.

$$\frac{d}{dt} \frac{\partial \mathcal{L}}{\partial \dot{\theta}_p} - \frac{\partial \mathcal{L}}{\partial \theta_p} = 0 \tag{7}$$

Some intermediate equations are then used to solve the Euler–Lagrange equation. They are shown in Eqs. (8)–(11).

$$\begin{aligned} \frac{\partial \mathcal{L}}{\partial \theta_p} = m_p \cdot \Big(& -\dot{x}_t \cdot L_w \cdot \dot{\theta}_p \cdot s_{\theta_p} \\ & + \dot{z}_t \cdot L_w \cdot \dot{\theta}_p \cdot c_{\theta_p} - g \cdot L_w \cdot s_{\theta_p} \Big) \end{aligned} \tag{8}$$

$$\frac{\partial \mathcal{L}}{\partial \dot{\theta}_p} = m_p \cdot \left(L_w^2 \cdot \dot{\theta}_p + \dot{x}_t \cdot L_w \cdot c_{\theta_p} + \dot{z}_t \cdot L_w \cdot s_{\theta_p} \right) \tag{9}$$

$$\begin{aligned} \frac{d}{dt} \frac{\partial \mathcal{L}}{\partial \dot{\theta}_p} = m_p \cdot \Big(& L_w^2 \cdot \ddot{\theta}_p + \ddot{x}_t \cdot L_w \cdot c_{\theta_p} - \dot{x}_t \cdot L_w \cdot \dot{\theta}_p \cdot s_{\theta_p} \\ & + \ddot{z}_t \cdot L_w \cdot s_{\theta_p} + \dot{z}_t \cdot L_w \cdot \dot{\theta}_p \cdot c_{\theta_p} \Big) \end{aligned} \tag{10}$$

$$\begin{aligned} \frac{d}{dt} \frac{\partial \mathcal{L}}{\partial \dot{\theta}_p} - \frac{\partial \mathcal{L}}{\partial \theta_p} = m_p \cdot \Big(& L_w^2 \cdot \ddot{\theta}_p + \ddot{x}_t \cdot L_w \cdot c_{\theta_p} \\ & + \ddot{z}_t \cdot L_w \cdot s_{\theta_p} + g \cdot L_w \cdot s_{\theta_p} \Big) \end{aligned} \tag{11}$$

The Euler–Lagrange equation can then be solved with respect to $\ddot{\theta}_p$ to give the describing differential equation of the payload, shown in Eq. (12). It is clear that the payload angle is dependent on the motion in both x- and z-direction, facilitating 2-DOF anti-swing control. The impact of the wire length L_w is also prominent, allowing for gain scheduling in the controller.

$$\ddot{\theta}_p = \frac{1}{L_w} \cdot \left(-\ddot{x}_t \cdot c_{\theta_p} - \ddot{z}_t \cdot s_{\theta_p} - g \cdot s_{\theta_p} \right) \tag{12}$$

3.2. Joint space kinematics

The joint space kinematics describes the relation between the joint angles and Cartesian coordinates of the crane tip. Fig. 8 shows the geometry which is used with the Denavit–Hartenberg parameters, where both booms are horizontal. The distances between consecutive joints are shown in Table 2. The Denavit–Hartenberg parameters are shown in Table 3, where **R** and **T** are rotational and translational matrices, respectively. The angles θ_m and θ_k denote the rotation about the main joint and knuckle joint, respectively.

The transformation matrix $\mathbf{A}_{DH}$ from the base of the crane to the tip of the crane can be established as a sequence of transformations based on the Denavit–Hartenberg parameters, shown in Eq. (13).

$$\begin{aligned} \mathbf{A}_{DH} = & \mathbf{T}_z(l_{1z}) \cdot \mathbf{T}_x(-l_{1x}) \cdot \mathbf{R}_x(90°) \cdot \mathbf{R}_z(\theta_m) \\ & \cdot \mathbf{R}_x(-90°) \cdot \mathbf{T}_z(l_{2z}) \cdot \mathbf{T}_x(l_{2x}) \cdot \mathbf{R}_x(90°) \\ & \cdot \mathbf{R}_z(\theta_k) \cdot \mathbf{R}_x(-90°) \cdot \mathbf{T}_z(-l_{3z}) \cdot \mathbf{T}_x(l_{3x}) \end{aligned} \tag{13}$$

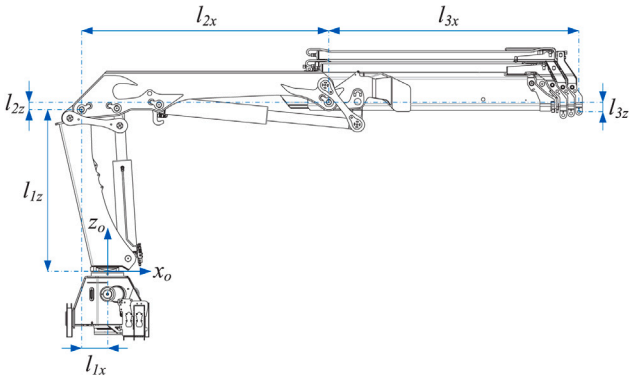

Fig. 8. Crane geometry used with Denavit–Hartenberg parameters.

Table 2
Coordinates shown in Fig. 8.

Name	Length [m]
l_{1x}	0.250
l_{1z}	1.569
l_{2x}	2.400
l_{2z}	0.070
l_{3x}	2.429
l_{3z}	0.093

Table 3
Denavit–Hartenberg parameters.

R_z	T_z	T_x	R_x
0	l_{1z}	$-l_{1x}$	90°
θ_m	0	0	−90°
0	l_{2z}	l_{2x}	90°
θ_k	0	0	−90°
0	$-l_{3z}$	l_{3x}	0

The final matrix $\mathbf{A}_{DH}$ is shown in Eq. (14).

$$\mathbf{A}_{DH} = \begin{bmatrix} c_{\theta_m+\theta_k} & 0 & -s_{\theta_m+\theta_k} & x_t \\ 0 & 1 & 0 & 0 \\ s_{\theta_m+\theta_k} & 0 & c_{\theta_m+\theta_k} & z_t \\ 0 & 0 & 0 & 1 \end{bmatrix} \tag{14}$$

$$\begin{aligned} x_t = & -l_{1x} + l_{2x} \cdot c_{\theta_m} - l_{2z} \cdot s_{\theta_m} \\ & + l_{3x} \cdot c_{\theta_m+\theta_k} + l_{3z} \cdot s_{\theta_m+\theta_k} \end{aligned} \tag{15}$$

$$\begin{aligned} z_t = & l_{1z} + l_{2x} \cdot s_{\theta_m} + l_{2z} \cdot c_{\theta_m} \\ & + l_{3x} \cdot s_{\theta_m+\theta_k} - l_{3z} \cdot c_{\theta_m+\theta_k} \end{aligned} \tag{16}$$

The joint kinematics from the crane base to the crane tip are now contained in x_t and z_t.

To find the correlation between the desired crane tip velocities and the joint velocities, the inverse Jacobian matrix must be defined. The correlation between crane tip velocities and joint velocities is shown in Eqs. (17) and (18).

$$\begin{bmatrix} \dot{x}_t \\ \dot{z}_t \end{bmatrix} = \mathbf{J} \cdot \begin{bmatrix} \dot{\theta}_m \\ \dot{\theta}_k \end{bmatrix} \tag{17}$$

$$\begin{bmatrix} \dot{\theta}_m \\ \dot{\theta}_k \end{bmatrix} = \mathbf{J}^{-1} \cdot \begin{bmatrix} \dot{x}_t \\ \dot{z}_t \end{bmatrix} \tag{18}$$

First, the Jacobian matrix is defined as the partial derivative of the crane tip position with respect to the joint angles, shown in Eq. (19).

$$\mathbf{J} = \begin{bmatrix} \frac{\partial}{\partial \theta_m}(x_t) & \frac{\partial}{\partial \theta_k}(x_t) \\ \frac{\partial}{\partial \theta_m}(z_t) & \frac{\partial}{\partial \theta_k}(z_t) \end{bmatrix} \tag{19}$$

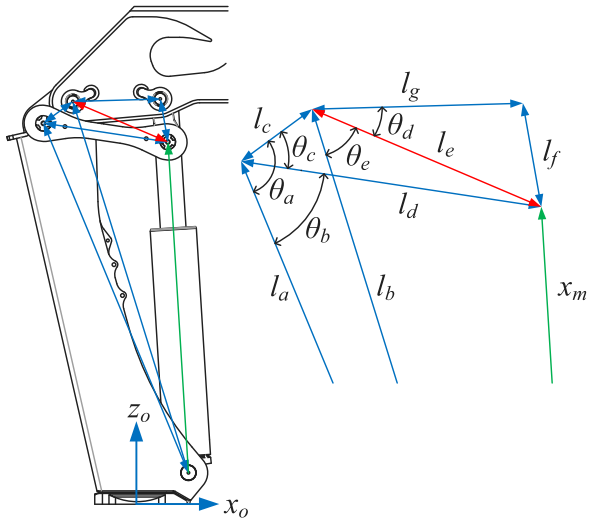

Fig. 9. Geometry of the linkage system for the main joint.

Table 4
Lengths of the main linkage.

Name	Length [m]
l_a	1.473
l_b	1.514
l_c	0.143
l_d	0.490
l_f	0.170
l_g	0.340

Inverting the Jacobian matrix yields the solution for the joint velocities, shown in Eqs. (20)–(22). The full calculations are shown in Appendix A.

$$\mathbf{J}^{\dagger} \triangleq \mathbf{J}^{-1} = \begin{bmatrix} J_{11}^{\dagger} & J_{12}^{\dagger} \\ J_{21}^{\dagger} & J_{22}^{\dagger} \end{bmatrix} \tag{20}$$

$$\dot{\theta}_m = J_{11}^{\dagger} \cdot \dot{x}_t + J_{12}^{\dagger} \cdot \dot{z}_t \tag{21}$$

$$\dot{\theta}_k = J_{21}^{\dagger} \cdot \dot{x}_t + J_{22}^{\dagger} \cdot \dot{z}_t \tag{22}$$

3.3. Actuator space kinematics

The actuator space kinematics describes the relation between the cylinder lengths and joint angles, where the joint angles are functions of the cylinder lengths, $\theta_m(x_m)$ and $\theta_k(x_k)$. Fig. 9 shows the geometry of the linkage system for the main joint. The coordinate x_m is the length of the hydraulic cylinder, and the length l_e is an intermediate length to help derive the actuator space kinematics. The lengths of the main linkage system are shown in Table 4.

The calculations of the actuator space kinematics are based on the law of cosines, since the linkage contains five triangles when the intermediate length l_e is introduced. An offset angle $\tilde{\theta}_m = 1.3$ rad is subtracted from the joint angle θ_m to ensure that the main boom is horizontal when $\theta_m = 0$. The calculations are shown in Eqs. (23)–(28), and the main joint angle θ_m is defined in Eq. (29). The calculations for the knuckle joint are given in Appendix B.

$$\theta_a = \arccos\left(\frac{l_a^2 + l_c^2 - l_b^2}{2 \cdot l_a \cdot l_c}\right) \tag{23}$$

$$\theta_b = \arccos\left(\frac{l_a^2 + l_d^2 - x_m^2}{2 \cdot l_a \cdot l_d}\right) \tag{24}$$

$$\theta_c = \theta_a - \theta_b \tag{25}$$

$$l_e = \sqrt{l_c^2 + l_d^2 - 2 \cdot l_c \cdot l_d \cdot c_{\theta_c}} \tag{26}$$

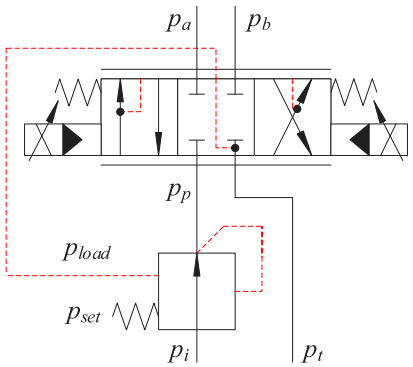

Fig. 10. Pressure compensated directional valve.

$$\theta_d = \arccos\left(\frac{l_e^2 + l_g^2 - l_f^2}{2 \cdot l_e \cdot l_g}\right) \tag{27}$$

$$\theta_e = \arccos\left(\frac{l_b^2 + l_e^2 - x_m^2}{2 \cdot l_b \cdot l_e}\right) \tag{28}$$

$$\theta_m = \theta_d + \theta_e - \tilde{\theta}_m \tag{29}$$

Based on Eq. (29), an analytical expression for $\dot{x}_m$ can be derived. This is done by taking the time derivative of $\theta_m(x_m)$, and then inverting to obtain an expression for $\dot{x}_m$. This is shown in Eq. (30). The full derivation of the cylinder velocity is given in Appendix C.

$$\dot{x}_m = \left(\frac{\partial \theta_m(x_m)}{\partial x_m}\right)^{-1} \cdot \dot{\theta}_m = \theta_{x_m}^{\dagger} \cdot \dot{\theta}_m \tag{30}$$

3.4. Hydraulic modeling

Both the main cylinder and the knuckle cylinder are controlled by pressure compensated directional valves. An illustration is shown in Fig. 10. The pressure compensator senses the load pressure to keep the pressure drop over the directional valve constant, thus ensuring a load independent flow. The governing equations of the pressure compensator are given in Eqs. (31)–(33).

$$u_{pc} = \frac{p_{set} + p_{load} - p_p}{\Delta p_c} \tag{31}$$

$$p_{load} = \begin{cases} p_a & \text{if } u_{spool} > 0 \\ p_b & \text{if } u_{spool} < 0 \\ p_t & \text{otherwise} \end{cases} \tag{32}$$

$$Q_{pc} = k_{pc} \cdot u_{pc} \cdot \sqrt{p_i - p_p} \tag{33}$$

where;

u_{pc}	= opening of compensator, $0 \leq u_{pc} \leq 1$
p_p	= compensated pressure at port p
Δp_c	= pressure difference when fully opened
p_a	= pressure at port a
p_b	= pressure at port b
p_t	= tank pressure
p_{set}	= spring pressure setting
p_{load}	= load pressure
u_{spool}	= position of the main spool, $-1 \leq u_{spool} \leq 1$
Q_{pc}	= flow in pressure compensator
k_{pc}	= flow gain of compensator
p_i	= compensator inlet pressure

The steady state of p_p is then given by Eq. (34).

$$p_p = p_{load} + p_{set} \tag{34}$$

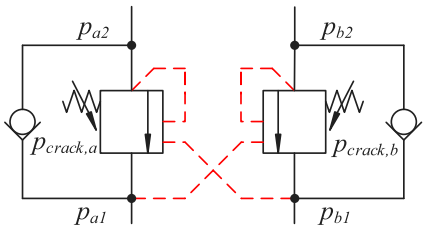

Fig. 11. Double counterbalance valves.

The sensing of the load pressures p_a and p_b ensures that the pressure drop over the directional control valve always equals p_{set}, and that the flow is load independent. This is shown in Eq. (35).

$$\begin{aligned} Q &= k_v \cdot u_{spool} \cdot \sqrt{p_p - p_{load}} \\ &= k_v \cdot u_{spool} \cdot \sqrt{p_{set}} \\ &= Q_{max} \cdot u_{spool} \end{aligned} \tag{35}$$

where;

k_v = flow gain of the directional valve
Q_{max} = maximum valve flow

To assist with load holding, lowering of the load, and protection against pressure surges, counterbalance valves are used between the directional valve and the hydraulic cylinder. Fig. 11 shows an illustration of double counterbalance valves, as used on the knuckle cylinder. The main cylinder uses a single counterbalance valve.

The governing equations of the counterbalance valves are shown in Eqs. (36) and (37).

$$u_a = \frac{p_{a2} + \psi \cdot p_{b1} - p_{crack,a}}{\Delta p_{CBV}} \tag{36}$$

$$u_b = \frac{p_{b2} + \psi \cdot p_{a1} - p_{crack,b}}{\Delta p_{CBV}} \tag{37}$$

where;

u_a = opening of valve a, $0 \leq u_a \leq 1$
u_b = opening of valve b, $0 \leq u_b \leq 1$
p_{a1} = pressure at valve a input side
p_{a2} = pressure at valve a actuator side
p_{b1} = pressure at valve b input side
p_{b2} = pressure at valve b actuator side
$p_{crack,a}$ = crack pressure of valve a
$p_{crack,b}$ = crack pressure of valve b
ψ = pilot area ratio
Δp_{CBV} = pressure difference when fully opened

The models of the pressure compensated directional valve and counterbalance valves are implemented using the hydraulics library in Simscape for the simulation purposes.

4. Control system design

From Eq. (12), it is clear that motion in both the x- and z-direction affects the payload angle dynamics. As such, the controller can utilize $\cos(\theta_p)$ and $\sin(\theta_p)$ for the motion in x- and z-direction to suppress the payload angle. The measured payload angle θ_p is used as feedback to generate crane tip velocities, as this eliminates the payload angle in steady state. As the function from control signal to crane tip motion is highly nonlinear, the kinematic functions derived earlier must be used. The full control system is shown in Fig. 12, outlining the feedback controller (blue), feedforward controller (red), and anti-swing controller (green). The anti-swing controller uses actuator kinematics (Act. Kin.), inverse Jacobian (Inv. Jac.), and inverse actuator kinematics (Inv. Act.).

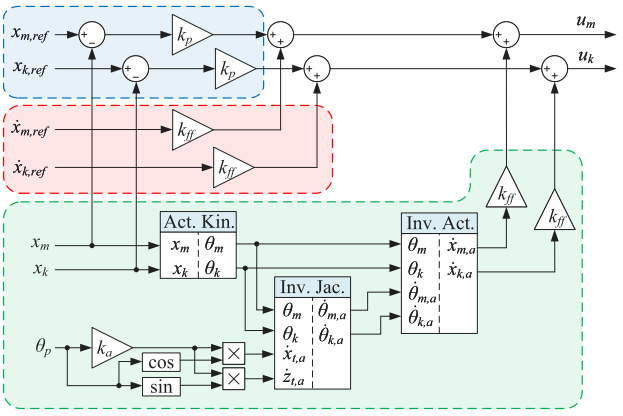

Fig. 12. Schematic of the proposed control system, with feedback controller (blue), feedforward controller (red), and anti-swing controller (green). (For interpretation of the references to color in this figure legend, the reader is referred to the web version of this article.)

Both the feedforward controller and anti-swing controller use the gain k_{ff} to calculate the valve opening from actuator velocity.

The control of the hydraulic cylinders uses feedback of the position error, and feedforward based on the velocity reference. Since the hydraulic system yields load independent velocity control, feedforward is an effective control method, as stated in [23] and [25]. The anti-swing gain k_a and the payload angle θ_p are used to generate two anti-swing crane tip velocities, $\dot{x}_{t,a}$ and $\dot{z}_{t,a}$ in order to suppress the payload angle. These velocities are transformed into joint space and then into actuator space, to yield the anti-swing cylinder velocities $\dot{x}_{m,a}$ and $\dot{x}_{k,a}$ for 2-DOF control. This is shown in Eqs. (38)–(42).

$$\dot{x}_{t,a} = \theta_p \cdot k_a \cdot \cos(\theta_p) \tag{38}$$

$$\dot{z}_{t,a} = \theta_p \cdot k_a \cdot \sin(\theta_p) \tag{39}$$

$$\begin{bmatrix} \dot{\theta}_{m,a} \\ \dot{\theta}_{k,a} \end{bmatrix} = \mathbf{J}^{\dagger} \cdot \begin{bmatrix} \dot{x}_{t,a} \\ \dot{z}_{t,a} \end{bmatrix} \tag{40}$$

$$\dot{x}_{m,a} = \theta^{\dagger}_{x_k} \cdot \dot{\theta}_{m,a} \tag{41}$$

$$\dot{x}_{k,a} = \theta^{\dagger}_{x_k} \cdot \dot{\theta}_{k,a} \tag{42}$$

The anti-swing cylinder velocities $\dot{x}_{m,a}$ and $\dot{x}_{k,a}$ are then multiplied by k_{ff} to generate the valve opening. The control outputs for the control system are shown in Eqs. (43) and (44).

$$u_m = (x_{m,ref} - x_m) \cdot k_{p,m} + \dot{x}_{m,ref} \cdot k_{ff,m} + \dot{x}_{m,a} \cdot k_{ff,m} \tag{43}$$

$$u_k = (x_{k,ref} - x_k) \cdot k_{p,k} + \dot{x}_{k,ref} \cdot k_{ff,k} + \dot{x}_{k,a} \cdot k_{ff,k} \tag{44}$$

4.1. Theoretical closed loop analysis

An analysis of the closed loop hanging load dynamics can be conducted based on the open loop hanging load dynamics and the selected control law. The control law controls the velocity of the crane tip. Recalling from earlier sections, the open loop dynamics and control law are given as:

$$\ddot{\theta}_p = \frac{1}{L_w} \cdot \left(-\ddot{x}_t \cdot c_{\theta_p} - \ddot{z}_t \cdot s_{\theta_p} - g \cdot s_{\theta_p} \right) \tag{45}$$

$$\dot{x}_t = \theta_p \cdot k_a \cdot c_{\theta_p} \tag{46}$$

$$\dot{z}_t = \theta_p \cdot k_a \cdot s_{\theta_p} \tag{47}$$

The expressions for $\ddot{x}_t$ and $\ddot{z}_t$ can be made by taking the time derivative of the crane tip velocities.

$$\ddot{x}_t = \dot{\theta}_p \cdot k_a \cdot (c_{\theta_p} - \theta_p \cdot s_{\theta_p}) \tag{48}$$

$$\ddot{z}_t = \dot{\theta}_p \cdot k_a \cdot (s_{\theta_p} + \theta_p \cdot c_{\theta_p}) \tag{49}$$

The closed loop hanging load dynamics can now be described as:

$$\ddot{\theta}_p = \frac{1}{L_w}\cdot\Big(-\dot{\theta}_p\cdot k_a\cdot(c_{\theta_p} - \theta_p\cdot s_{\theta_p})\cdot c_{\theta_p} \\ -\dot{\theta}_p\cdot k_a\cdot(s_{\theta_p} + \theta_p\cdot c_{\theta_p})\cdot s_{\theta_p} - g\cdot s_{\theta_p}\Big) \tag{50}$$

Linearization is conducted to analyze the damping that the control law provides. Linearizing around $\theta_p \approx 0$ yields:

$$\dot{x}_t = \theta_p\cdot k_a \tag{51}$$

$$\dot{z}_t = 0 \tag{52}$$

$$\ddot{x}_t = \dot{\theta}_p\cdot k_a \tag{53}$$

$$\ddot{z}_t = 0 \tag{54}$$

$$\ddot{\theta}_p = -\frac{\dot{\theta}_p\cdot k_a}{L_w} - \frac{g\cdot\theta_p}{L_w} \tag{55}$$

A Laplace transform of the linearized closed loop hanging load dynamics is conducted to find the damping ratio of the system. The closed loop hanging load dynamics is a second order system, given by:

$$s^2\cdot\theta_p = -\frac{s\cdot\theta_p\cdot k_a}{L_w} - \frac{g\cdot\theta_p}{L_w} \tag{56}$$

$$s^2 + \frac{s\cdot k_a}{L_w} + \frac{g}{L_w} = 0 \tag{57}$$

$$s^2 + 2\cdot s\cdot\zeta\cdot\omega + \omega^2 = 0 \tag{58}$$

The bandwidth and damping ratio of the linearized system are calculated as:

$$\omega = \sqrt{\frac{g}{L_w}} \tag{59}$$

$$\zeta = \frac{k_a}{2\cdot\sqrt{L_w\cdot g}} \tag{60}$$

It can be seen that the damping ratio ζ increases as the anti-swing gain k_a increases, and that the system is stable with $k_a > 0$. An analytical expression for the anti-swing gain can now be calculated based on desired damping ratio and wire length by rearranging Eq. (60).

$$k_a = 2\cdot\zeta\cdot\sqrt{L_w\cdot g} \tag{61}$$

The analytical expressions in Eqs. (50) and (61) are used in a numerical analysis of the closed loop nonlinear dynamics. A set of transient simulations with $L_w = 2$ m and initial conditions of $\theta_{p,0} = 0.1$ rad and $\dot{\theta}_{p,0} = 0$ rad/s are shown in Fig. 13 to showcase the damping that the anti-swing controller provides. To numerically analyze the performance of the anti-swing controller, the RMS value of θ_p as a function of ζ from the transient simulations is shown in Fig. 14. The minimum is at $\zeta \approx 0.5$, equating to $k_a \approx 4.5$ m/s.

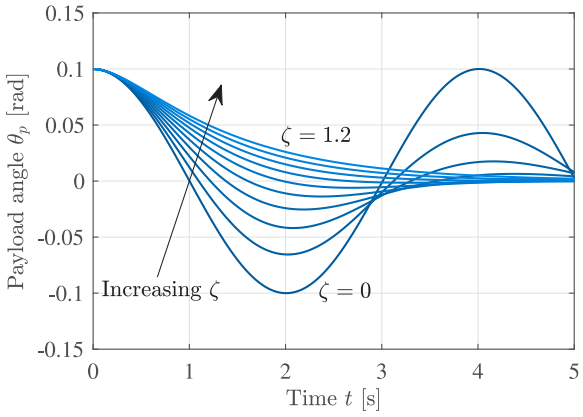

Fig. 13. Transient simulation of closed loop nonlinear hanging load dynamics with damping ratio $0 < \zeta < 1.2$.

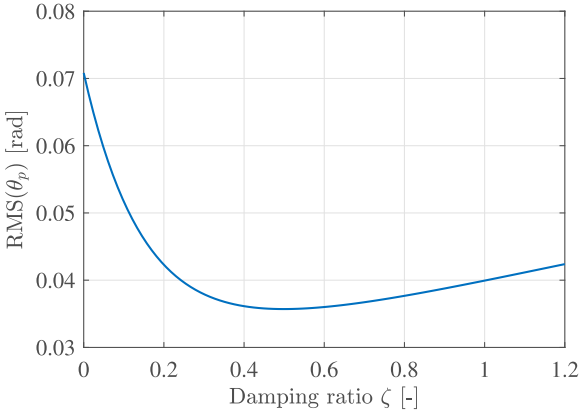

Fig. 14. RMS(θ_p) as a function of damping ratio for the closed loop nonlinear hanging load dynamics.

Table 5
Simulation parameters.

Description	Name	Value
Main feedback	$k_{p,m}$	5 m^{-1}
Main out-stroke feedforward	$k^+_{ff,m}$	30.16 s m^{-1}
Main in-stroke feedforward	$k^-_{ff,m}$	18.37 s m^{-1}
Knuckle feedback	$k_{p,k}$	20 m^{-1}
Knuckle out-stroke feedforward	$k^+_{ff,k}$	26.51 s m^{-1}
Knuckle in-stroke feedforward	$k^-_{ff,k}$	14.72 s m^{-1}
Wire length	L_w	2 m

5. System simulation

The system simulation is conducted in MATLAB Simscape™ with imported CAD models and the models derived in Section 3. For the position control, a path controller based on a trapezoidal velocity reference is used, as described in [25]. The path controller operates in actuator space, and uses segments of constant cylinder velocity. The relevant parameters for the simulation are shown in Table 5. Fig. 15 shows the cylinder position references for the simulation.

A comparison is made in Fig. 16, which shows the payload angle θ_p with $k_a = 0$ m/s and $k_a = 5$ m/s. The anti-swing controller eliminates the constant oscillations in the payload angle θ_p when the cylinder is running with constant velocity, and reduces the payload angle when the crane tip is accelerating. The anti-swing controller is effective for both in-stroke and out-stroke cylinder motion.

Fig. 17 shows the position error during simulation with and without anti-swing control. The position error is larger with the anti-swing controller, but reducing the payload angle θ_p is a higher priority than reducing the position error. Although the position error is higher when using anti-swing control, it goes towards zero after the payload angle is suppressed.

Fig. 18 shows the control signals for the feedback controller $u_{k,fb}$, feedforward controller $u_{k,ff}$, and anti-swing controller $u_{k,a}$ on the knuckle cylinder during simulation with $k_a = 5$ m/s. The main control signal u_k is without large oscillations, which is advantageous for the flexible loader crane. The contributions of the anti-swing controller can be seen as small spikes when the cylinders are accelerating, i.e. when the control signal is not constant.

To evaluate the effect of the wire length L_w, the crane is simulated with different wire lengths and anti-swing gains. From Eq. (12) it is shown that the payload angle dynamics is dependent on the inverse of the wire length L_w. To compensate for this a gain scheduling of k_a can be made to be a function of the wire length. A gain scheduling of the anti-swing gain equivalent to Eq. (61) with $\zeta = 0.5644$ is used for this simulation. This equates to $k_a = 5$ m/s at $L_w = 2$ m. This

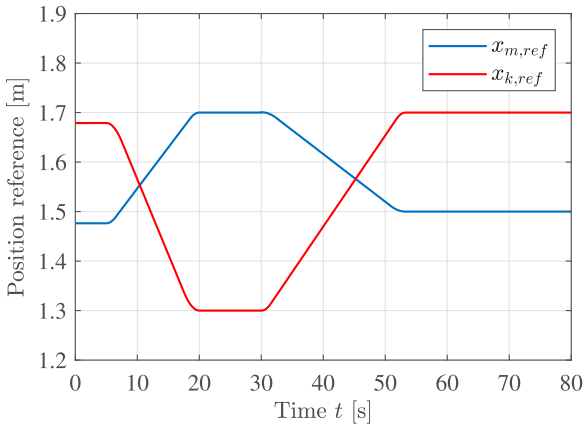

Fig. 15. Position reference for cylinders during simulation.

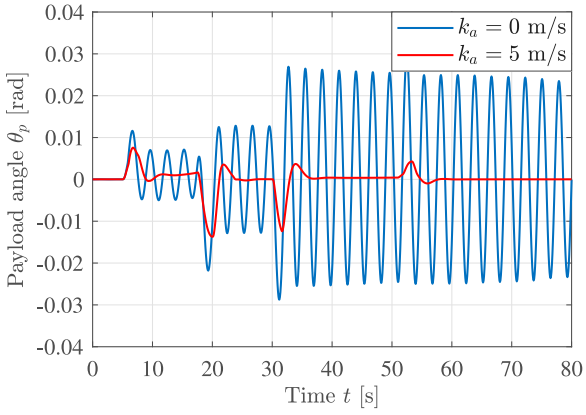

Fig. 16. Payload angle θ_p with (red line) and without (blue line) anti-swing control. (For interpretation of the references to color in this figure legend, the reader is referred to the web version of this article.)

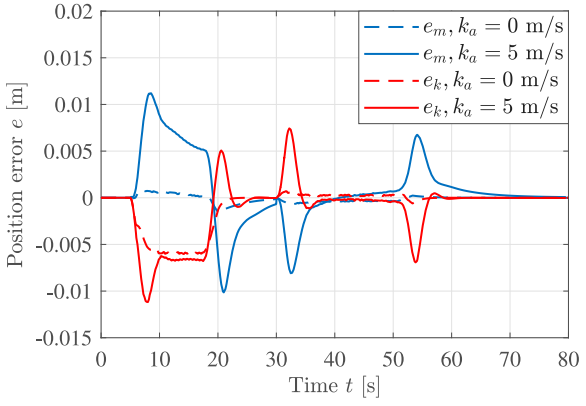

Fig. 17. Cylinder position error with (solid line) and without (dashed line) anti-swing control.

means that the wire length L_w needs to be measured in a practical application. The payload angle during motion for different wire lengths is shown in Fig. 19. The control system yields good suppression of the payload angle and eliminates the constant oscillations for the different wire lengths.

To evaluate the interaction between the position controller and anti-swing controller and identify any instability, a simulation is carried out with higher values of the anti-swing gain k_a. The payload angle is shown in Fig. 20 and the main cylinder position error is shown in

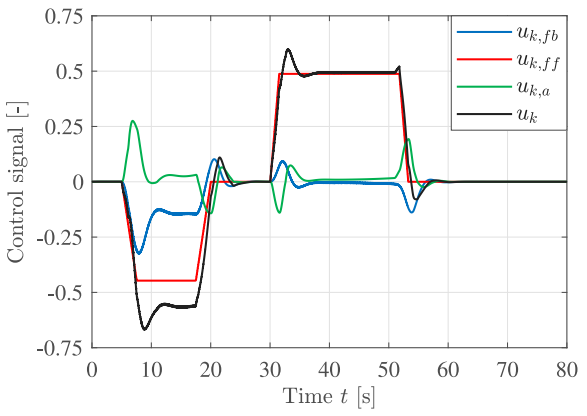

Fig. 18. Control signals for the knuckle cylinder with anti-swing control.

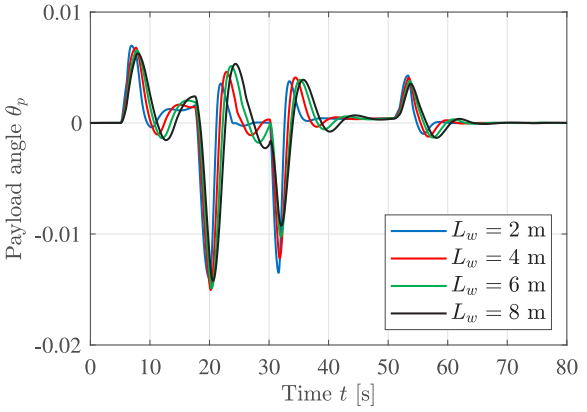

Fig. 19. Payload angle for different wire lengths L_w.

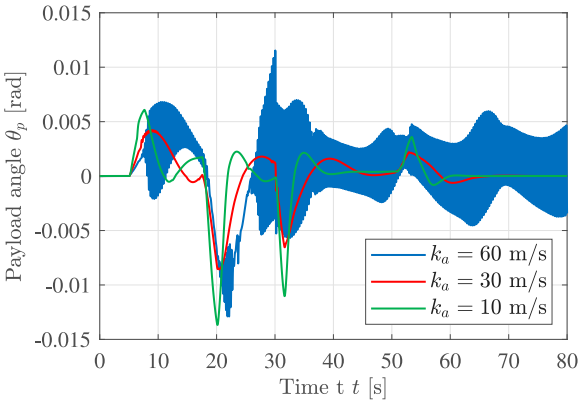

Fig. 20. Payload angle θ_p for different anti-swing gains k_a.

Fig. 21. Increasing the gain improves performance until oscillations appear in the nonlinear system. In Fig. 20 this is illustrated with three different gains where the oscillatory behavior is pronounced a k_a = 60 m/s.

6. Experimental results

The anti-swing controller is implemented on a CompactRIO on the HMF 2020K4 loader crane. A picture of the test setup is shown in Fig. 22. The sensor used in the experiments is the BNO055 Absolute Orientation Sensor from Bosch Sensortec. It outputs three Euler angles and they are all used to calculate the payload angle θ_p.

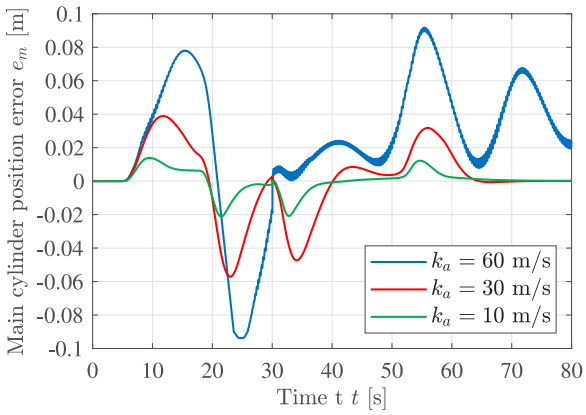

Fig. 21. Main cylinder position error e_m for different anti-swing gains k_a.

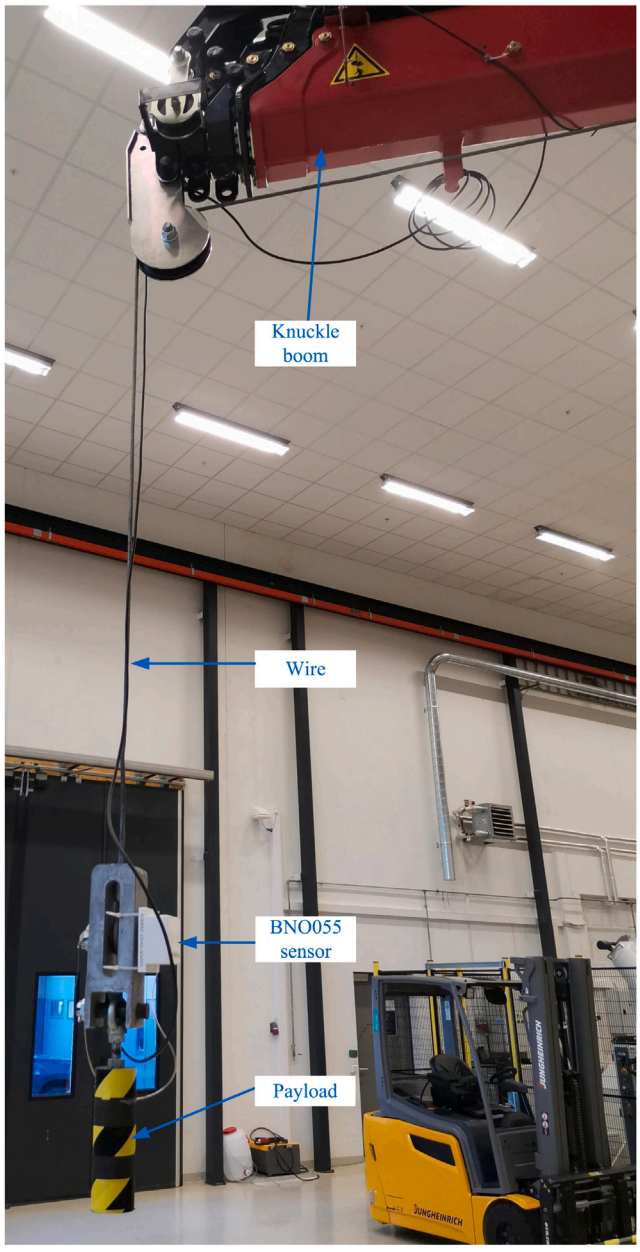

Fig. 22. HMF 2020K4 crane in laboratory.

Table 6
Identified deadband for each actuator.

Actuator	Out, u^+	In, u^-
Main	0.24	−0.22
Knuckle	0.20	−0.31

There is some deadband in the valves on the HMF 2020K4 loader crane, and therefore deadband compensation has been implemented for the laboratory experiments. The identified deadbands for the valves are shown in Table 6. The equation for the deadband compensation is shown in Eq. (62). By adding a small deadband $\tilde{u}$, it is ensured that the valve will be able to stay closed when no movement is needed.

$$\hat{u} = \begin{cases} u^+ + (1-u^+)\cdot u & \text{if } u > \tilde{u} \\ u^- + (1+u^-)\cdot u & \text{if } u < -\tilde{u} \\ 0 & \text{otherwise} \end{cases} \tag{62}$$

where;

$\hat{u}$ = compensated control signal
u = control signal
u^+ = out-stroke deadband
u^- = in-stroke deadband
$\tilde{u}$ = desired deadband, 0.001

In the laboratory there was identified some drift in the payload angle sensor. This has been removed with a digital high pass filter, which is shown in Eqs. (63) and (64).

$$y_i = \alpha \cdot y_{i-1} + \alpha \cdot (x_i - x_{i-1}) \tag{63}$$

$$\alpha = \frac{T_f}{T_f + T_s} \tag{64}$$

where;

i = sample number
y = filter output
x = filter input
T_f = filter time constant
T_s = sample time, 0.01 s

To avoid filtering out the motion of the payload, the filter time constant T_f should be larger than the pendulum period T_p. The pendulum period is calculated based on the wire length, shown in Eq. (65).

$$T_p = 2 \cdot \pi \cdot \sqrt{\frac{L_w}{g}} = 2.837 \text{ s} \tag{65}$$

Because of the value of T_p the filter time constant has been set to $T_f = 3$ s. The effects of the drift and the implemented high pass filter is shown in Fig. 23. The payload angle drifted towards an offset of 0.02 rad. With the drift of the payload angle, the position error for the main cylinder converged to a large value. With the high pass filter the drift of the payload angle has been removed, and the position error converges to zero as expected.

In the laboratory experiments two different paths are used. The first path is equal to the path in the simulations shown in Fig. 15, while the second path is used to show experimental results and performance in another configuration. An illustration of the crane and the crane tip motion in the xz-plane for the two paths is shown in Fig. 24. The first path is shown in blue, and the second path is shown in red. The circles denote the starting position of the crane tip for each path and then the crane moves back and forth along the path.

As in the simulations, the payload angle has been plotted for different gains using the first path. This is shown in Fig. 25. Larger gains yielded better suppression and removed the constant oscillations. However, the system became unstable with anti-swing gain $k_a \geq 7$ m/s and the experiment was stopped.

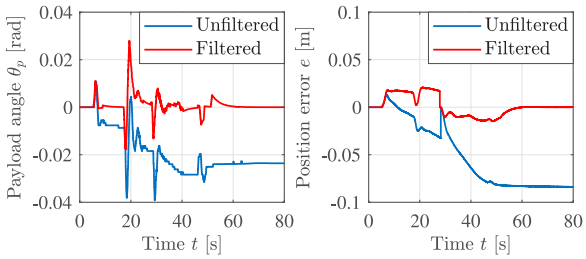

(a) Drift of payload angle. (b) Main cylinder position error.

Fig. 23. Payload angle drift and its effect on the position error for the main cylinder.

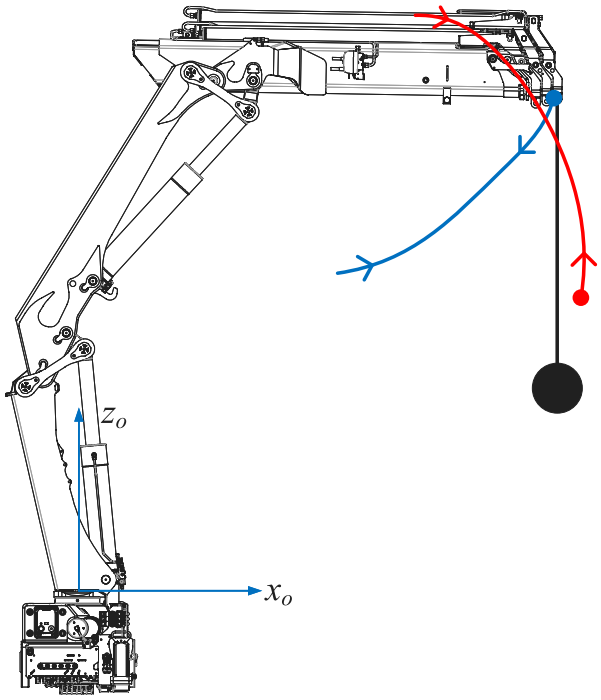

Fig. 24. Crane tip motion in the xz-plane for the first path (blue) and second path (red) in the laboratory. (For interpretation of the references to color in this figure legend, the reader is referred to the web version of this article.)

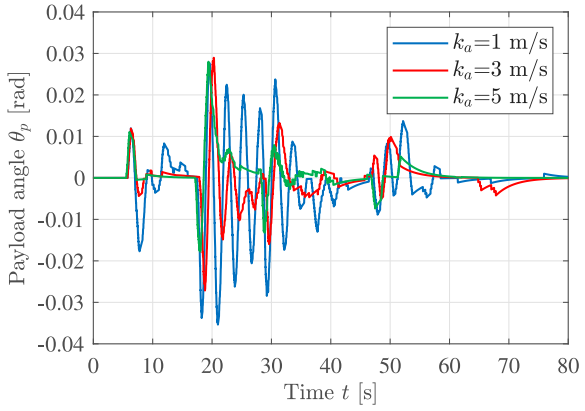

Fig. 25. Payload angle θ_p for different anti-swing gains k_a.

A plot of the payload angle with and without anti-swing is shown in Fig. 26. The payload experiences large oscillations without the anti-swing controller. With the controller, the payload angle is significantly reduced.

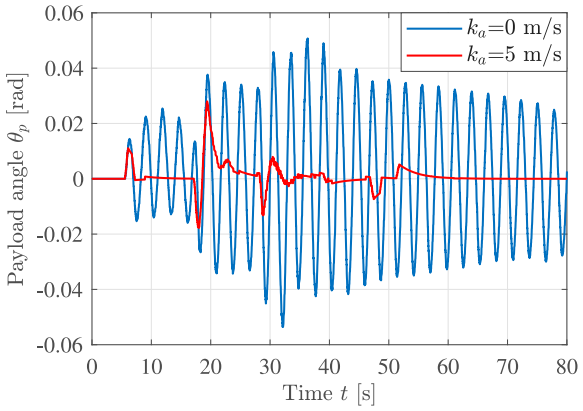

Fig. 26. Payload angle θ_p with (red line) and without (blue line) anti-swing control during the first path. (For interpretation of the references to color in this figure legend, the reader is referred to the web version of this article.)

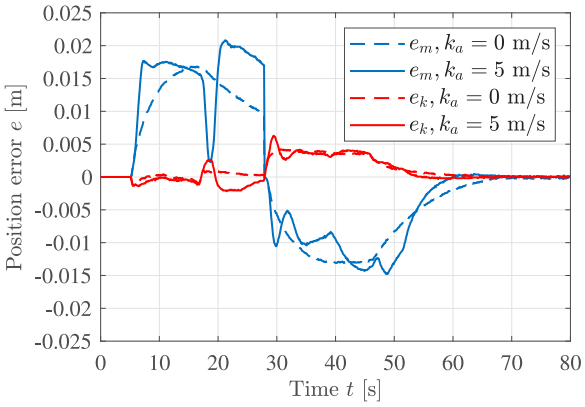

Fig. 27. Cylinder position error with (solid line) and without (dashed line) anti-swing control.

The position error with and without anti-swing is shown in Fig. 27. The position error with anti-swing control is kept close to the position error without control, showing that the anti-swing controller is able to suppress the payload angle without a large impact on the position error. The position error without anti-swing control is larger compared to the ideal system in the simulations.

The payload angle θ_p during the motion along the second path is shown in Fig. 28. The control system yields good suppression of the payload angle for this configuration also. Due to the vertical crane tip motion during the first few seconds of the second path, the payload barely oscillates in this segment.

7. Conclusion

In this paper a novel anti-swing controller for hydraulic cranes is designed utilizing load independent velocity control. The anti-swing controller is simulated, evaluated, and experimentally verified on a hydraulic loader crane. Relevant kinematic functions are derived to enable control of the payload angle. The motion control system operates in actuator space, and controls the two hydraulic cylinders in order to suppress the payload angle during motion. The kinematic functions are used to transform the feedback of the payload angle θ_p into a command signal for the valves.

In the simulations, the feedback gain k_a is evaluated in order to suppress the payload angle θ_p during motion. Simulation results show significant reduction in the payload angle and elimination of oscillations during a motion with constant cylinder velocity. This is achieved

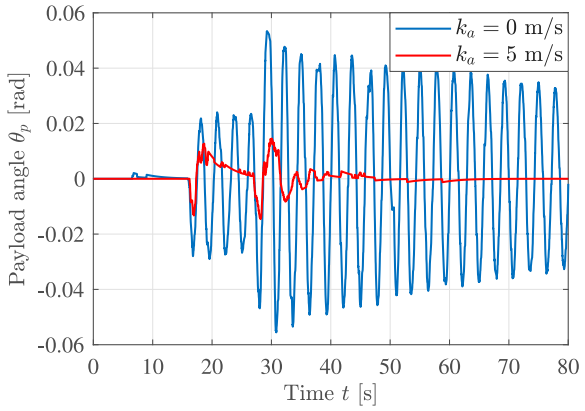

Fig. 28. Payload angle θ_p with (red line) and without (blue line) anti-swing control during the second path. (For interpretation of the references to color in this figure legend, the reader is referred to the web version of this article.)

Table 7
Lengths of the knuckle linkage.

Name	Length [m]
l_h	1.626
l_i	1.650
l_j	0.168
l_k	0.490
l_m	0.220
l_n	0.280

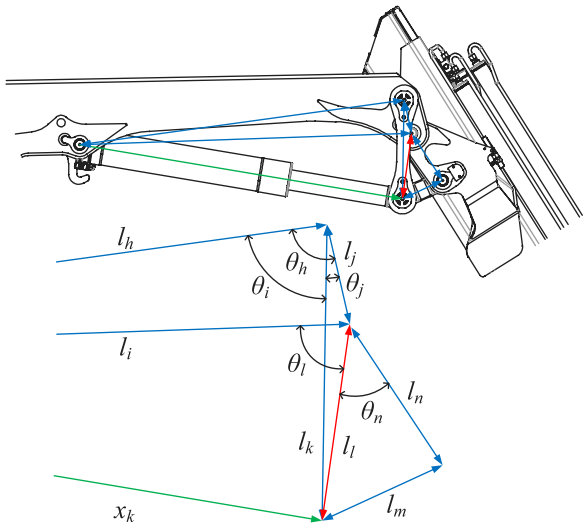

Fig. 29. Geometry of the linkage system for the knuckle joint.

without larger cylinder position errors or oscillations in the control signal. Simulation results verify the performance of the anti-swing controller.

In the laboratory, a high pass filter is added to eliminate sensor drift. A deadband compensator is used to compensate for the deadband in the valves. The feedback gain k_a is also evaluated, and the experimental verification shows that the anti-swing controller successfully suppresses the payload angle, with similar results as in the simulations. Results in the laboratory showcase the feasibility of the novel anti-swing controller for hydraulic cranes in a practical application.

Future work may include extending the anti-swing controller to include the slewing motion of the crane, which will include deriving the necessary kinematic functions. Actively controlling the wire length with a winch can also be added, and may include gain scheduling based on the wire length. Modeling of the flexibility of the crane may also be included to analyze how this interacts with the payload dynamics, and how this affects the performance of the anti-swing control system.

CRediT authorship contribution statement

Konrad Johan Jensen: Conceptualization, Methodology, Software, Validation, Formal analysis, Investigation, Resources, Data curation, Writing - original draft, Writing - review & editing. **Morten Kjeld Ebbesen:** Conceptualization, Methodology, Resources, Writing - review & editing, Supervision. **Michael Rygaard Hansen:** Conceptualization, Methodology, Resources, Writing - review & editing, Supervision.

Declaration of competing interest

The authors declare that they have no known competing financial interests or personal relationships that could have appeared to influence the work reported in this paper.

Funding

This work was supported by the Norwegian Ministry of Education and Research grant number 155597.

Appendix A. Jacobian matrix and inverse Jacobian

Recalling the transformation matrix $\mathbf{A}_{DH}$ and the crane tip positions x_t and z_t as:

$$\mathbf{A}_{DH} = \begin{bmatrix} c_{\theta_m+\theta_k} & 0 & -s_{\theta_m+\theta_k} & x_t \\ 0 & 1 & 0 & 0 \\ s_{\theta_m+\theta_k} & 0 & c_{\theta_m+\theta_k} & z_t \\ 0 & 0 & 0 & 1 \end{bmatrix} \tag{A.1}$$

$$\begin{aligned} x_t = &-l_{1x} + l_{2x}\cdot c_{\theta_m} - l_{2z}\cdot s_{\theta_m} \\ &+ l_{3x}\cdot c_{\theta_m+\theta_k} + l_{3z}\cdot s_{\theta_m+\theta_k} \end{aligned} \tag{A.2}$$

$$\begin{aligned} z_t = &\, l_{1z} + l_{2x}\cdot s_{\theta_m} + l_{2z}\cdot c_{\theta_m} \\ &+ l_{3x}\cdot s_{\theta_m+\theta_k} - l_{3z}\cdot c_{\theta_m+\theta_k} \end{aligned} \tag{A.3}$$

The Jacobian matrix is defined as the partial derivative of the crane tip position with respect to the joint angles, shown in Eqs. (A.4)–(A.8).

$$\mathbf{J} = \begin{bmatrix} \frac{\partial}{\partial\theta_m}(x_t) & \frac{\partial}{\partial\theta_k}(x_t) \\ \frac{\partial}{\partial\theta_m}(z_t) & \frac{\partial}{\partial\theta_k}(z_t) \end{bmatrix} \tag{A.4}$$

$$\begin{aligned} \frac{\partial}{\partial\theta_m}(x_t) = &-l_{2x}\cdot s_{\theta_m} - l_{2z}\cdot c_{\theta_m} \\ &- l_{3x}\cdot s_{\theta_m+\theta_k} + l_{3z}\cdot c_{\theta_m+\theta_k} \end{aligned} \tag{A.5}$$

$$\frac{\partial}{\partial\theta_k}(x_t) = l_{3x}\cdot s_{\theta_m+\theta_k} - l_{3z}\cdot c_{\theta_m+\theta_k} \tag{A.6}$$

$$\begin{aligned} \frac{\partial}{\partial\theta_m}(z_t) = &\, l_{2x}\cdot c_{\theta_m} - l_{2z}\cdot s_{\theta_m} \\ &+ l_{3x}\cdot c_{\theta_m+\theta_k} + l_{3z}\cdot s_{\theta_m+\theta_k} \end{aligned} \tag{A.7}$$

$$\frac{\partial}{\partial\theta_k}(z_t) = -l_{3x}\cdot c_{\theta_m+\theta_k} - l_{3z}\cdot s_{\theta_m+\theta_k} \tag{A.8}$$

Inverting the Jacobian matrix yields the solution for the joint velocities, shown in Eqs. (A.9)–(A.15).

$$\mathbf{J}^\dagger \triangleq \mathbf{J}^{-1} = \begin{bmatrix} J_{11}^\dagger & J_{12}^\dagger \\ J_{21}^\dagger & J_{22}^\dagger \end{bmatrix} \tag{A.9}$$

$$\dot{\theta}_m = J_{11}^\dagger\cdot\dot{x}_t + J_{12}^\dagger\cdot\dot{z}_t \tag{A.10}$$

$$\dot{\theta}_k = J_{21}^\dagger\cdot\dot{x}_t + J_{22}^\dagger\cdot\dot{z}_t \tag{A.11}$$

$$J_{11}^\dagger = \frac{-l_{3x}\cdot c_{\theta_m+\theta_k} - l_{3z}\cdot s_{\theta_m+\theta_k}}{l_{2x}\cdot l_{3z}\cdot c_{\theta_k} + l_{3x}\cdot l_{2z}\cdot c_{\theta_k} - l_{2x}\cdot l_{3x}\cdot s_{\theta_k} + l_{2z}\cdot l_{3z}\cdot s_{\theta_k}} \tag{A.12}$$

$$J_{12}^{\dagger} = \frac{-l_{3x}\cdot s_{\theta_m+\theta_k}+l_{3z}\cdot c_{\theta_m+\theta_k}}{l_{2x}\cdot l_{3z}\cdot c_{\theta_k}+l_{3x}\cdot l_{2z}\cdot c_{\theta_k}-l_{2x}\cdot l_{3x}\cdot s_{\theta_k}+l_{2z}\cdot l_{3z}\cdot s_{\theta_k}} \tag{A.13}$$

$$J_{21}^{\dagger} = \frac{-l_{2x}\cdot c_{\theta_m}+l_{2z}\cdot s_{\theta_m}-l_{3x}\cdot c_{\theta_m+\theta_k}-l_{3z}\cdot s_{\theta_m+\theta_k}}{l_{2x}\cdot l_{3z}\cdot c_{\theta_k}+l_{3x}\cdot l_{2z}\cdot c_{\theta_k}-l_{2x}\cdot l_{3x}\cdot s_{\theta_k}+l_{2z}\cdot l_{3z}\cdot s_{\theta_k}} \tag{A.14}$$

$$J_{22}^{\dagger} = \frac{-l_{2x}\cdot s_{\theta_m}-l_{2z}\cdot c_{\theta_m}-l_{3x}\cdot s_{\theta_m+\theta_k}+l_{3z}\cdot c_{\theta_m+\theta_k}}{l_{2x}\cdot l_{3z}\cdot c_{\theta_k}+l_{3x}\cdot l_{2z}\cdot c_{\theta_k}-l_{2x}\cdot l_{3x}\cdot s_{\theta_k}+l_{2z}\cdot l_{3z}\cdot s_{\theta_k}} \tag{A.15}$$

Appendix B. Actuator space kinematics

To calculate the actuator space kinematics for the knuckle joint, the same procedure is followed as with the main joint. The geometry for the knuckle linkage is shown in Fig. 29. The coordinate x_k is the length of the hydraulic cylinder, and the length l_l is the intermediate length. The lengths of the knuckle linkage system are shown in Table 7.

As with the main joint, an offset angle $\tilde{\theta}_k = 3.1086$ rad is subtracted from the joint angle θ_k to ensure that the knuckle boom is horizontal when $\theta_m + \theta_k = 0$. The calculations are shown in Eqs. (B.1)–(B.6), and the knuckle joint angle θ_k is defined in Eq. (B.7).

$$\theta_h = \arccos\left(\frac{l_h^2+l_j^2-l_i^2}{2\cdot l_h\cdot l_j}\right) \tag{B.1}$$

$$\theta_i = \arccos\left(\frac{l_h^2+l_k^2-x_k^2}{2\cdot l_h\cdot l_k}\right) \tag{B.2}$$

$$\theta_j = \theta_h - \theta_i \tag{B.3}$$

$$l_l = \sqrt{l_j^2+l_k^2-2\cdot l_j\cdot l_k\cdot c_{\theta_j}} \tag{B.4}$$

$$\theta_n = \arccos\left(\frac{l_l^2+l_n^2-l_m^2}{2\cdot l_l\cdot l_n}\right) \tag{B.5}$$

$$\theta_l = \arccos\left(\frac{l_i^2+l_l^2-x_k^2}{2\cdot l_i\cdot l_l}\right) \tag{B.6}$$

$$\theta_k = \theta_n + \theta_l - \tilde{\theta}_k \tag{B.7}$$

Appendix C. Time derivative of actuator space kinematics

By taking the time derivative of the actuator space kinematics, expressions for the cylinder velocities $\dot{x}_m$ and $\dot{x}_k$ can be made. The equations for the knuckle joint are given below, but the procedure is the same for the main joint. Taking the time derivative of Eqs. (B.1)–(B.7) from Appendix B yields:

$$\dot{\theta}_h = 0 \tag{C.1}$$

$$\dot{\theta}_i = \frac{x_k}{l_h\cdot l_k\cdot\sqrt{1-\left(\frac{l_h^2+l_k^2-x_k^2}{2\cdot l_h\cdot l_k}\right)^2}}\cdot\dot{x}_k \tag{C.2}$$

$$\dot{\theta}_j = -\frac{x_k}{l_h\cdot l_k\cdot\sqrt{1-\left(\frac{l_h^2+l_k^2-x_k^2}{2\cdot l_h\cdot l_k}\right)^2}}\cdot\dot{x}_k \tag{C.3}$$

$$\begin{aligned}\dot{l}_l &= \left(l_j^2+l_k^2-2\cdot l_j\cdot l_k\cdot c_{\theta_j}\right)^{-\frac{1}{2}}\cdot l_j\cdot l_k\cdot s_{\theta_j}\cdot\dot{\theta}_j \\ &= -\frac{\left(l_j^2+l_k^2-2\cdot l_j\cdot l_k\cdot c_{\theta_j}\right)^{-\frac{1}{2}}\cdot l_j\cdot s_{\theta_j}\cdot x_k}{l_h\cdot\sqrt{1-\left(\frac{l_h^2+l_k^2-x_k^2}{2\cdot l_h\cdot l_k}\right)^2}}\cdot\dot{x}_k\end{aligned} \tag{C.4}$$

$$\begin{aligned}\dot{\theta}_n &= -\frac{l_l^2-l_n^2+l_m^2}{2\cdot l_l^2\cdot l_n\cdot\sqrt{1-\left(\frac{l_l^2+l_n^2-l_m^2}{2\cdot l_l\cdot l_n}\right)^2}}\cdot\dot{l}_l \\ &= \frac{\left(l_l^2-l_n^2+l_m^2\right)\cdot\left(l_j^2+l_k^2-2\cdot l_j\cdot l_k\cdot c_{\theta_j}\right)^{-\frac{1}{2}}\cdot l_j\cdot s_{\theta_j}\cdot x_k}{2\cdot l_l^2\cdot l_n\cdot l_h\cdot\sqrt{1-\left(\frac{l_l^2+l_n^2-l_m^2}{2\cdot l_l\cdot l_n}\right)^2}\cdot\sqrt{1-\left(\frac{l_h^2+l_k^2-x_k^2}{2\cdot l_h\cdot l_k}\right)^2}}\cdot\dot{x}_k\end{aligned} \tag{C.5}$$

$$\begin{aligned}\dot{\theta}_l &= \frac{-1}{\sqrt{1-\left(\frac{l_i^2+l_l^2-x_k^2}{2\cdot l_i\cdot l_l}\right)^2}}\cdot\frac{\dot{l}_l\cdot\left(l_l^2+x_k^2-l_i^2\right)-2\cdot l_l\cdot x_k\cdot\dot{x}_k}{2\cdot l_i\cdot l_l^2} \\ &= \frac{x_k}{l_i\cdot l_l\cdot\sqrt{1-\left(\frac{l_i^2+l_l^2-x_k^2}{2\cdot l_i\cdot l_l}\right)^2}}\cdot\dot{x}_k - \frac{l_l^2+x_k^2-l_i^2}{2\cdot l_i\cdot l_l^2\cdot\sqrt{1-\left(\frac{l_i^2+l_l^2-x_k^2}{2\cdot l_i\cdot l_l}\right)^2}}\cdot\dot{l}_l \\ &= \frac{x_k}{l_i\cdot l_l\cdot\sqrt{1-\left(\frac{l_i^2+l_l^2-x_k^2}{2\cdot l_i\cdot l_l}\right)^2}}\cdot\dot{x}_k \\ &\quad + \frac{\left(l_l^2+x_k^2-l_i^2\right)\cdot\left(l_j^2+l_k^2-2\cdot l_j\cdot l_k\cdot c_{\theta_j}\right)^{-\frac{1}{2}}\cdot l_j\cdot s_{\theta_j}\cdot x_k}{2\cdot l_i\cdot l_l^2\cdot l_h\cdot\sqrt{1-\left(\frac{l_i^2+l_l^2-x_k^2}{2\cdot l_i\cdot l_l}\right)^2}\cdot\sqrt{1-\left(\frac{l_h^2+l_k^2-x_k^2}{2\cdot l_h\cdot l_k}\right)^2}}\cdot\dot{x}_k\end{aligned} \tag{C.6}$$

$$\begin{aligned}\dot{\theta}_k &= \dot{\theta}_n + \dot{\theta}_l \\ &= \left(\frac{\left(l_l^2-l_n^2+l_m^2\right)\cdot\left(l_j^2+l_k^2-2\cdot l_j\cdot l_k\cdot c_{\theta_j}\right)^{-\frac{1}{2}}\cdot l_j\cdot s_{\theta_j}\cdot x_k}{2\cdot l_l^2\cdot l_n\cdot l_h\cdot\sqrt{1-\left(\frac{l_l^2+l_n^2-l_m^2}{2\cdot l_l\cdot l_n}\right)^2}\cdot\sqrt{1-\left(\frac{l_h^2+l_k^2-x_k^2}{2\cdot l_h\cdot l_k}\right)^2}} + \frac{x_k}{l_i\cdot l_l\cdot\sqrt{1-\left(\frac{l_i^2+l_l^2-x_k^2}{2\cdot l_i\cdot l_l}\right)^2}}\right. \\ &\quad \left. + \frac{\left(l_l^2+x_k^2-l_i^2\right)\cdot\left(l_j^2+l_k^2-2\cdot l_j\cdot l_k\cdot c_{\theta_j}\right)^{-\frac{1}{2}}\cdot l_j\cdot s_{\theta_j}\cdot x_k}{2\cdot l_i\cdot l_l^2\cdot l_h\cdot\sqrt{1-\left(\frac{l_i^2+l_l^2-x_k^2}{2\cdot l_i\cdot l_l}\right)^2}\cdot\sqrt{1-\left(\frac{l_h^2+l_k^2-x_k^2}{2\cdot l_h\cdot l_k}\right)^2}}\right)\cdot\dot{x}_k\end{aligned} \tag{C.7}$$

Solving Eq. (C.7) with respect to $\dot{x}_k$ yields:

$$\begin{aligned}\dot{x}_k &= \left(\frac{\left(l_l^2-l_n^2+l_m^2\right)\cdot\left(l_j^2+l_k^2-2\cdot l_j\cdot l_k\cdot c_{\theta_j}\right)^{-\frac{1}{2}}\cdot l_j\cdot s_{\theta_j}\cdot x_k}{2\cdot l_l^2\cdot l_n\cdot l_h\cdot\sqrt{1-\left(\frac{l_l^2+l_n^2-l_m^2}{2\cdot l_l\cdot l_n}\right)^2}\cdot\sqrt{1-\left(\frac{l_h^2+l_k^2-x_k^2}{2\cdot l_h\cdot l_k}\right)^2}} + \frac{x_k}{l_i\cdot l_l\cdot\sqrt{1-\left(\frac{l_i^2+l_l^2-x_k^2}{2\cdot l_i\cdot l_l}\right)^2}}\right. \\ &\quad \left. + \frac{\left(l_l^2+x_k^2-l_i^2\right)\cdot\left(l_j^2+l_k^2-2\cdot l_j\cdot l_k\cdot c_{\theta_j}\right)^{-\frac{1}{2}}\cdot l_j\cdot s_{\theta_j}\cdot x_k}{2\cdot l_i\cdot l_l^2\cdot l_h\cdot\sqrt{1-\left(\frac{l_i^2+l_l^2-x_k^2}{2\cdot l_i\cdot l_l}\right)^2}\cdot\sqrt{1-\left(\frac{l_h^2+l_k^2-x_k^2}{2\cdot l_h\cdot l_k}\right)^2}}\right)^{-1}\cdot\dot{\theta}_k\end{aligned} \tag{C.8}$$

References

[1] Lee Ho-Hoon, Cho Sung-Kun, Cho Jae-Sung. A new anti-swing control of overhead cranes. IFAC Proc Vol 1997;30(13):115–20, IFAC Workshop on Automation in the Steel Industry: Current Practice and Future Developments (ASI'97), Kyongju, Korea, 16–18 July 1997.

[2] Lee Ho-Hoon. Modeling and control of a three-dimensional overhead crane. J Dyn Syst Meas Control 1998;120(4):471–6.

[3] Cho Sung-Kun, Lee Ho-Hoon. An anti-swing control of a 3-dimensional overhead crane. In: Proceedings of the 2000 American control conference. (IEEE Cat. No. 00CH36334), vol. 2. 2000. p. 1037–41.

[4] Lee Ho-Hoon, Choi Seung-Gap. A model-based anti-swing control of overhead cranes with high hoisting speeds. In: Proceedings 2001 ICRA. IEEE international conference on robotics and automation (Cat. No. 01CH37164), vol. 3. 2001. p. 2547–52.

[5] Lee Ho-Hoon, Cho Sung-Kun. A new fuzzy-logic anti-swing control for industrial three-dimensional overhead cranes. In: Proceedings 2001 ICRA. IEEE international conference on robotics and automation (Cat. No. 01CH37164), vol. 3. 2001. p. 2956–61.

[6] Cho Sung-Kun, Lee Ho-Hoon. A fuzzy-logic antiswing controller for three-dimensional overhead cranes. ISA Trans 2002;41(2):235–43.

[7] Lee Ho-Hoon. A new approach for the anti-swing control of overhead cranes with high-speed load hoisting. Internat J Control 2003;76(15):1493–9.

[8] Fang Y, Dixon WE, Dawson DM, Zergeroglu E. Nonlinear coupling control laws for an underactuated overhead crane system. IEEE/ASME Trans Mechatronics 2003;8(3):418–23.

[9] Lee Ho-Hoon. A new design approach for the anti-swing trajectory control of overhead cranes with high-speed hoisting. Internat J Control 2004;77(10):931–40.

[10] Lee Ho-Hoon, Liang Yi, Segura Del. A sliding-mode antiswing trajectory control for overhead cranes with high-speed load hoisting. J Dyn Syst Meas Control 2006;128(4):842–5.

[11] Park Hahn, Chwa Dongkyoung, Hong Keum-Shik. A feedback linearization control of container cranes: Varying rope length. Int J Control Autom Syst 2007;5.

[12] Park M, Chwa D, Hong S. Antisway tracking control of overhead cranes with system uncertainty and actuator nonlinearity using an adaptive fuzzy sliding-mode control. IEEE Trans Ind Electron 2008;55(11):3972–84.
[13] Schindele D, Menn I, Aschemann H. Nonlinear optimal control of an overhead travelling crane. In: 2009 IEEE control applications, intelligent control. 2009. p. 1045–50.
[14] Lee Ho-Hoon, Liang Yi. A robust anti-swing trajectory control of overhead cranes with high-speed load hoisting: experimental study. In: ASME international mechanical engineering congress and exposition, vol. 8: dynamic systems and control, parts A and B. 2010. p. 711–6.
[15] Ngo QH, Hong K. Sliding-mode antisway control of an offshore container crane. IEEE/ASME Trans Mechatronics 2012;17(2):201–9.
[16] Ambrosino Michele, Dawans Arnaud, Thierens Brent, Garone Emanuele. Oscillation reduction for knuckle cranes. In: Proceedings of the 37th international symposium on automation and robotics in construction. Kitakyushu, Japan: International Association for Automation and Robotics in Construction (IAARC); 2020, p. 1590–7.
[17] Singhose WE, Seering Warren, Singer M. Input shaping for vibration reduction with specified insensitivity to modeling errors. In: Proc. Japan-USA symp. flexible automation, vol. 1. 1996.
[18] Sorensen Khalid L, Singhose William, Dickerson Stephen. A controller enabling precise positioning and sway reduction in bridge and gantry cranes. Control Eng Pract 2007;15(7):825–37, Special Issue on Award Winning Applications.
[19] Kjelland Magnus B, Hansen Michael R. Using input shaping and pressure feedback to suppress oscillations in slewing motion of lightweight flexible hydraulic crane. Int J Fluid Power 2015;16(3):141–8.
[20] Boschetti G, Richiedei D, Trevisani A. Delayed reference control for multi-degree-of-freedom elastic systems: Theory and experimentation. Control Eng Pract 2011;19(9):1044–55.
[21] Boschetti G, Caracciolo R, Richiedei D, Trevisani A. A non-time based controller for load swing damping and path-tracking in robotic cranes. J Intell Robot Syst 2014;76(2):201–17.
[22] Kjelland MB, Hansen MR, Tyapin I, Hovland G. Tool-point control of a planar hydraulically actuated manipulator with compensation of non-actuated degree of freedom. In: 2012 12th international conference on control, automation and systems. 2012. p. 672–7.
[23] Bak Morten Kollerup, Hansen Michael Rygaard. Analysis of offshore knuckle boom crane — Part two: Motion control. Model Identif Control 2013;34(4):175–81.
[24] Jensen Konrad Johan, Ebbesen Morten Kjeld, Hansen Michael Rygaard. Adaptive feedforward control of a pressure compensated differential cylinder. Appl Sci 2020;10(21):7847.
[25] Jensen Konrad Johan, Kjeld Ebbesen Morten, Rygaard Hansen Michael. Development of point-to-point path control in actuator space for hydraulic knuckle boom crane. Actuators 2020;9(2):27.
[26] Kjelland Magnus B, Tyapin Ilya, Hovland Geir, Hansen Michael R. Tool-point control for a redundant heave compensated hydraulic manipulator. In: Proceedings of the 2012 IFAC workshop on automatic control in offshore oil and gas production. Trondheim, Norway: Norwegian University of Science and Technology; 2012.

Konrad Johan Jensen received the M.Sc. degree in Mechatronics from the University of Agder, Norway, in 2015. His master's thesis focused on path control of hydraulic cranes. He is currently pursuing a doctorate degree in Mechatronics at the Department of Engineering Sciences at the University of Agder. His main research interests include hydraulic systems, robotics, optimization, and control systems.

Morten Kjeld Ebbesen is affiliated with the Department of Engineering Sciences, University of Agder, Norway, as an associate professor in the Mechatronics group. He received his M.Sc. (2003) and Ph.D. (2008) in mechanical engineering from the University of Aalborg, Denmark. His interests are dynamics, flexible multi-body systems, time-domain simulation, fluid power, and optimization.

Michael Rygaard Hansen received the M.Sc. in Mechanical Engineering, Aalborg University, 1989. Ph.D. in Computer-Aided Analysis and Design of Mechanical Mechanisms, Institute of Mechanical Engineering, Aalborg University, 1992. Main interests lie within the use of numerical methods for modeling, design and optimization of dynamic mechatronic systems. Teaching and supervision experience at B.Sc., M.Sc. and Ph.D. level since 1990. The courses have mainly been devoted to education within mechanical engineering.